Journal of Materials Chemistry A

REVIEW

View Article Online
View Journal | View Issue

Cite this: J. Mater. Chem. A, 2019, 7, 22730

MXene-engineered lithium–sulfur batteries

Zhubing Xiao,[ab] Zhonglin Li,[a] Xueping Meng[a] and Ruihu Wang *[a]

Received 6th August 2019
Accepted 10th September 2019

DOI: 10.1039/c9ta08600e

rsc.li/materials-a

Lithium–sulfur (Li–S) batteries are one of the promising next-generation energy storage systems. Tremendous efforts have been devoted to developing conductive nanoarchitectures for improving sulfur utilization and cycling stability. MXenes, a family of 2D transition metal carbides, nitrides and carbonitrides, have recently captured considerable attention in energy storage and conversion. Herein, we have summarized recent advances of MXene-based materials in the cathodes, anodes and separators of Li–S batteries and highlighted the theoretical and experimental importance of high polarity and rich surface chemistry in polysulfide trapping. Their superiority for suppressing polysulfide shuttling and improving sulfur utilization has been demonstrated. We have also concluded the perspectives and challenges that need to be addressed for MXene-based Li–S batteries and some new strategies have been proposed to improve the electrochemical performance, which shed light on future development of MXene-based materials in high-energy-density Li–S batteries.

1. Introduction

The energy crisis and environmental pollution have stimulated us to adopt electricity generated by clean energy sources, such as wind, solar, marsh gas and nuclear energy. Nevertheless, owing to the intermittent nature of these renewable energy sources, it is imperative to develop energy storage devices for their efficient utilization. In this context, electrochemical energy storage based on different redox reactions or the Faraday effect is of vital significance.[1–3] Lithium-ion batteries (LIBs) represent the most advanced commercial technology, but there is still a great gap between state-of-the-art energy density and ever-growing demands from advancing markets of portable electronics, electric vehicles and stationary storage devices. Meanwhile, the relatively high cost and latent safety issues of LIBs also hinder their large scale applications in electric vehicles. Therefore, exploring alternative high-energy electrochemical systems is required for a paradigm change in energy storage.[4–7]

[a]State Key Laboratory of Structural Chemistry, Fujian Institute of Research on the Structure of Matter, Chinese Academy of Sciences, Fuzhou, Fujian 350002, China. E-mail: ruihu@fjirsm.ac.cn

[b]Henan Key Laboratory of Photovoltaic Materials, Henan University, Kaifeng, 475004, China

Zhubing Xiao is a research associate at the Fujian Institute of Research on the Structure of Matter, Chinese Academy of Sciences. He received his bachelor degree from Hunan Agricultural University in 2012, master degree from Wenzhou University in 2015, and PhD from the Fujian Institute of Research on the Structure of Matter, University of Chinese Academy of Sciences in 2019. His research focuses on the synthesis of nanostructured materials, including carbon-based composites, metal sulfides/carbides, and their applications in the field of high-energy-density lithium–sulfur batteries.

Zhonglin Li is a research assistant at the Fujian Institute of Research on the Structure of Matter, Chinese Academy of Sciences. He received his bachelor degree from the North University of China in 2016 and master degree from the Fujian Institute of Research on the Structure of Matter, University of Chinese Academy of Sciences in 2019. His research focuses on MOF-derived composites and their applications in the field of high-energy-density lithium–sulfur batteries.

Among a variety of alternative technologies, lithium–sulfur (Li–S) batteries take a leading stand for the development of advanced energy storage systems. The multielectron reactions between elemental sulfur and lithium deliver a high theoretical gravimetric energy density of 2600 W h kg^{-1}, greatly outperforming LIBs (Fig. 1a).[8–10] Besides, sulfur is naturally abundant, cost effective and nontoxic, and it is produced in large quantities daily as a byproduct in petroleum refining, which endows great possibility for industrial applications.[11,12] Some advanced battery companies like Oxis Energy and Sion Power have made their first step in the commercialization of sulfur-based energy systems,[13,14] but Li–S battery technology still faces some critical challenges leading to poor cycling lifespan and shelf life, and these issues drastically hinder the step towards mass production and large-scale commercialization.

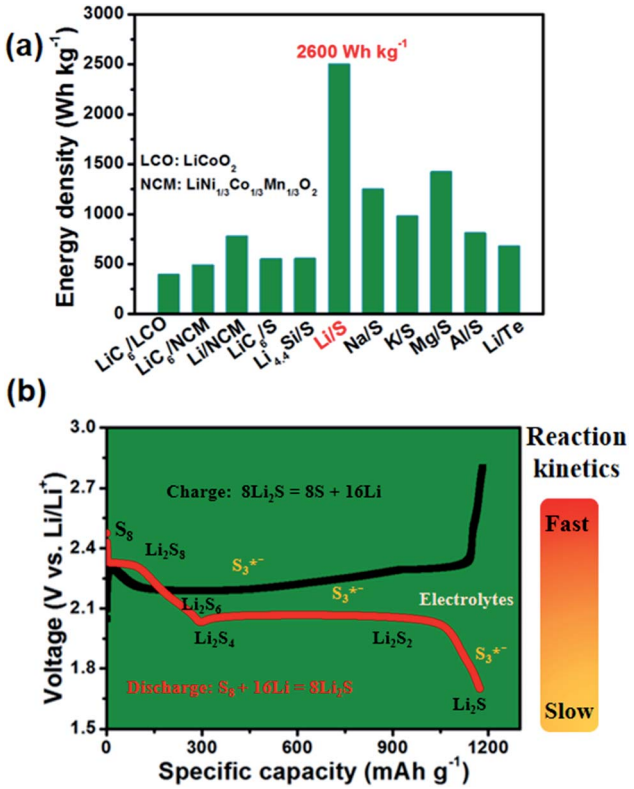

Fig. 1 (a) Schematic comparison of the theoretical energy densities of various rechargeable battery systems. (b) Representative charge/discharge voltage profile based on the stoichiometric redox chemistry between lithium and sulfur.

It has been known that elemental sulfur exists primarily in the form of an eight-membered ring (S_8) under ambient conditions. During cycling, S_8 electrochemically undergoes multistage changes with the formation of high-order lithium polysulfide (LiPS) intermediates that are soluble in organic ether electrolytes (Fig. 1b). The electric field and concentration gradient force could drive LiPS to migrate from the cathode region to the lithium anode region through porous separators. The soluble LiPS could diffuse back to the cathode side during charging and is re-oxidized to sulfur, but the arbitrary LiPS migration induces not only the loss of the active materials and deposition of insoluble sulfides (Li_2S_2/Li_2S) on the cathode surface, but also severe contamination/passivation of the lithium anode. The notorious shuttle effect is the origin of the low coulombic efficiency and severe self-discharge behavior in Li–S batteries. Apart from LiPS shuttling, there are other major concerns related to the inherent characteristics of sulfur. Both sulfur and its solid discharge products are electronically and ionically insulating, greatly constraining efficient electrochemical utilization of the active materials. In addition, the density difference between sulfur (2.03 g cm^{-3}) and Li_2S (1.67 g cm^{-3}) entails large volumetric fluctuation ($\approx$80%) during lithiation/delithiation, which has important effects on the cathode structure and integrity.[15,16]

The above-mentioned problems make it a tougher challenge to assemble high-energy-density Li–S batteries with both high sulfur content and high areal sulfur loading. The increases in sulfur content and areal sulfur loading are not just a simple

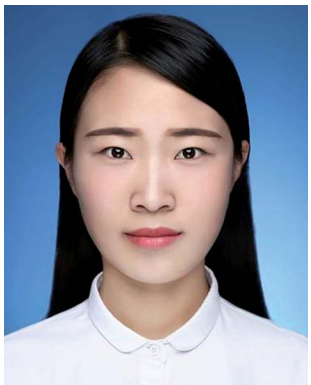

Xueping Meng is a graduate at Fujian Normal University. She received her bachelor degree from Taishan University in 2018. Her research focuses on porous organic polymer-derived carbon composites and their applications in the field of high-energy-density lithium–sulfur batteries.

Ruihu Wang received his bachelor degree from Qufu Normal University in 1998 and his PhD in physical chemistry from the Fujian Institute of Research on the Structure of Matter, Chinese Academy of Sciences in 2004. From 2004 to 2008, he worked as a postdoctoral fellow at the Department of Chemistry, University of Idaho and the Center for of Environmentally Benign Catalysis, University of Kansas. He joined Research on the Structure of Matter, Chinese Academy of Sciences as a professor in 2008. His research interests mainly focus on porous organic polymers for catalysis and energy storage.

addition algorithm, they will exaggerate the existing problems and putting some regular electrode-modification strategies under further inspection. More sophisticated strategies are in demand to efficiently promote the electrochemical performance without plaguing the overall energy density of Li–S batteries. Recently, it has become popular to rationally introduce polar anchoring materials (AMs), such as transition metal oxides, sulfides, carbides, phosphides and borides, into the cell configurations for constructing high-energy-density Li–S batteries.[17–23] Transition metal carbides, carbonitrides and nitrides (MXenes) are promising candidates because of their unique 2D structure, high conductivity and rich surface functionality.[24–26] With the ever-increasing attention to emerging 2D materials beyond graphene and the compositional versatility of their parent MAX phases (Fig. 2b), more than thirty MXenes, including $Ti_3C_2T_x$, V_2CT_x, Nb_2CT_x and $Nb_4C_3T_x$ (T_x represents functional groups on the surface, such as –O, –OH and –F), have been successfully synthesized so far, with more predicted to exist according to theoretical calculations.[22,23] Moreover, the increasing number of publications of MXene-based Li–S batteries clearly show their potential in Li–S batteries (Fig. 2a). Although MXenes have been mentioned in recent reviews of high-performance electrode materials for energy storage,[15,24–26] there is no comprehensive summary in MXene-engineered Li–S batteries hitherto. A timely and systematic review on MXene-based materials is expected to further accelerate the development of emerging materials and promote their application in high-energy-density Li–S batteries.

Herein, we summarize the foremost theoretical findings and experimental advances of MXene-based materials in cathodes, anodes and separators of Li–S batteries (Fig. 3) and systematically illustrate the relationships between the intrinsic properties of MXenes and chemical interactions with LiPS and the subsequent effects on the electrochemical performance. Moreover, the challenges for their application in Li–S batteries have been proposed. A guiding route towards the rational design of MXene-based Li–S batteries with high sulfur utilization and high life has been provided.

2. Structure and synthesis of MXenes

In general, MXenes originate from their layered precursors, ternary carbides and nitrides (MAX phases), by selectively etching the A layers. The chemical formula of MXenes is $M_{n+1}X_nT_x$, where M refers to transition metals, including Sc, Ti, Zr, Hf, V, Nb, Ta, Cr and Mo; A means group IIIA or IVA elements; X refers to C and N; and n is 1, 2 and 3 (Fig. 2b).[22,23] Similar to their MAX precursors, the metal atoms in MXenes are arranged in a close-packed mode, and C and N atoms fill the octahedral interstitial sites (Fig. 2c). The overall crystal structure of MXenes can be classified into a hexagonal close-packed structure, but the ordering of M atoms changes from M_2XT_x to $M_3X_2T_x$ and $M_4X_3T_x$. The M atoms in M_2XT_x follow ABABAB ordering, while the M atoms in $M_3X_2T_x$ and $M_4X_3T_x$ exhibit ABCABC ordering. The atomic ordering is very important for the synthesis of various MXenes. Notably, when the MAX phases are etched with HF, an accordion-like structure composed of multi-layered stacked MXene nanosheets could be obtained. However, the MAX phases are exfoliated by intercalation with Li^+ ions when LiF/HCl was used as the etchant, giving rise to few-layered

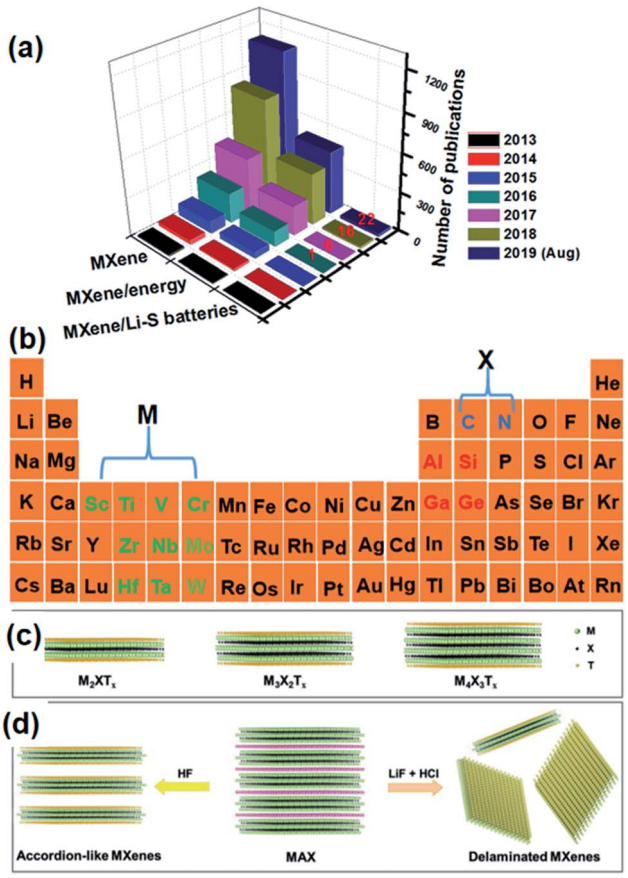

Fig. 2 (a) The number of recent publications on MXene-based Li–S batteries. Source: Web of Science, searching index: [topic = MXene or MXene energy or MXene Li–S batteries]. (b) Fragment of the periodic table showing the elements forming MAX phases with the general composition $M_{n+1}AX_n$ (n = 1, 2, or 3). (c) Structures of MXenes with three different formulas. (d) Synthesis of accordion-like MXenes by HF etching and delaminated MXenes by LiF/HCl etching. Reproduced with permission.[32] Copyright 2018, WILEY-VCH.

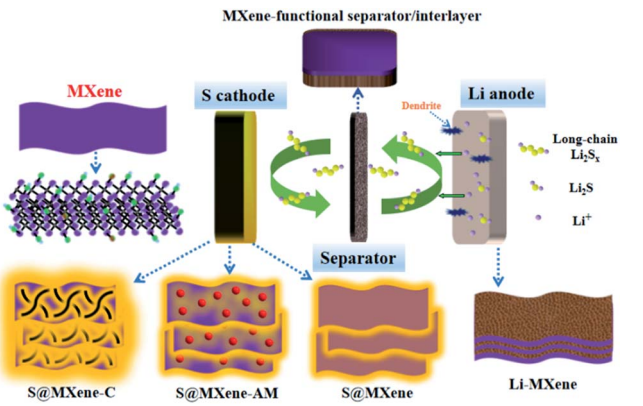

Fig. 3 Illustration of the MXene-engineered sulfur cathode, Li anode and separator in Li–S batteries.

MXene nanosheets (Fig. 2d). In addition, MXenes are highly hydrophilic and could be readily dispersed in water and the majority of polar organic solvents owing to abundant surface termination. Meanwhile, both the electron-deficient metal center and polar functional groups on the atomic surface are favorable for the binding of LiPS intermediates, which enables efficient LiPS adsorbents.[15,24–26]

3. Theoretical study on MXenes-based Li–S batteries

Recently, a wide spectrum of studies have been reported on developing sulfur host materials with strong chemical interactions toward LiPS along with mechanistic investigation of the underlying principles of these materials.[17] Due to the interactive surface and high conductivity, MXenes are attractive candidates for AMs for the sulfur cathode.[26] It is of scientific and technological importance to have a detailed understanding of their basic properties and potential applications. We will make a brief summary of representative theoretical findings of Li–S batteries based on uniformly or non-uniformly functionalized MXenes (Fig. 4).

3.1 Uniformly functionalized MXenes

3.1.1 OH-functionalized MXenes. The Ti_2CT_x MXene phase was first employed as the sulfur host material by Nazar's group in 2015.[27] They have proposed the surface reactivity of Ti_3C_2 and Ti_3CN MXenes after interacting with LiPS species using a combination of X-ray photoelectron spectroscopy (XPS) analysis and density functional theory (DFT) calculations. It has been certified that prior to Ti–S bond formation *via* Lewis acid–base interactions, the terminal –OH groups on the Ti_3C_2 and Ti_3CN MXenes are gradually consumed by the trapped LiPS through the formation of thiosulfate/polythionate intermediates. Rao and co-workers have further demonstrated the attractive interactions between S from the polysulfide chain and H from –OH groups, which contribute to the binding between LiPS and OH-terminated MXenes and thus enhance the entrapment of sulfur species in the cathode region of Li–S batteries.[28] However, MXenes are usually synthesized from a MAX phase by etching Al or Si with aqueous HF or HCl/LiF solution, and –F, –OH and –O groups are simultaneously introduced into the surface of MXenes during etching.[22] It is difficult to determine if one dominates or more groups work together. Therefore, it is paramount to clarify the anchoring mechanism of these termination groups toward LiPS for guiding the experimental research of MXenes.

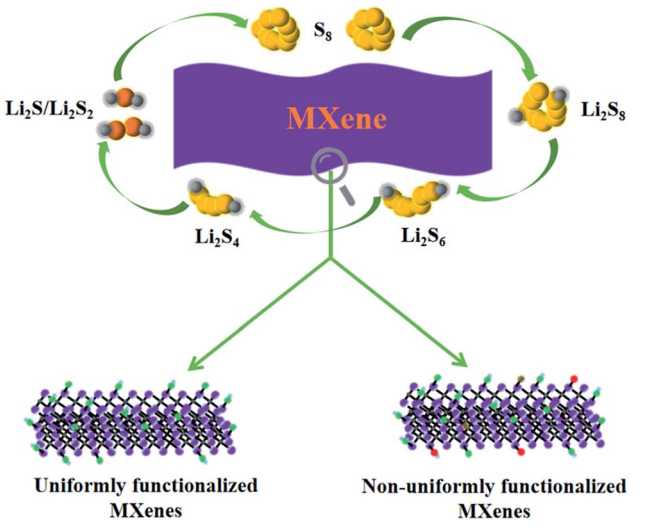

Fig. 4 Illustration of theoretical findings of Li–S batteries based on uniformly or non-uniformly functionalized MXenes.

3.1.2 O/F-functionalized MXenes. Surface terminations of MXenes largely depend on the etching and post-synthetic treatment conditions.[22,23] Although there are some discrepancies in determining the concentration of termination groups by different techniques, such as XPS and NMR, it is widely accepted that –F and –O are dominant surface functional groups in these MXenes. The binding energy, bond characteristics and electron transfer on the surface of –O or –F uniformly functionalized MXenes have been recently investigated.[28–35] As a great demonstration, Zhao and co-workers have systematically disclosed the anchoring effects of O-terminated Ti_3C_2 and Ti_2C MXenes for LiPS (Fig. 5a).[29] Benefiting from the attractions between Li^+ in LiPS and O atoms in the Ti_2CO_2 and $Ti_3C_2O_2$ monolayer, the O-terminated MXenes could bond with LiPS with moderate binding strength to effectively stabilize soluble LiPS. This lithiophilic (Li–O bonding) behavior coupled with sulfiphilic behavior (Ti–S bonding) suggests the amphipathicity of MXenes toward LiPS. Fan and co-workers have thoroughly investigated chemical interactions between LiPS species and six $M_3C_2O_2$-typed MXenes (M = Cr, V, Ti, Nb, Hf and Zr) (Fig. 5b). Similar to Ti_2CO_2, obvious Li–O interactions between $M_3C_2O_2$ MXenes and LiPS have been validated. A monotonic relationship between the binding energies and lattice constants of $M_3C_2O_2$ has been identified, suggesting that a smaller lattice constant is apt to induce stronger binding capability to LiPS.[30] More recently, Wei and co-workers have comprehensively investigated the synergetic effects of binding capability with LiPS and the catalytic effects for the delithiation process of Li_2S based on Ti_3C_2 MXenes (Fig. 5c).[31] According to their results, O- and S-terminated Ti_3C_2 could serve as optimal host materials for sulfur cathodes, echoing with Zhao's report.[29]

By applying O-functionalized Ti_2N and F-functionalized Ti_2N as substrates, Lin and co-workers have demonstrated that both Ti_2NO_2 and Ti_2NF_2 not only possess moderate adsorption energies toward LiPS (Fig. 5b),[32] but also achieve good balance between adsorption energies and intactness of LiPS. Moreover, supported by the density of states for S_8, Li_2S_8, Li_2S_6, Li_2S_4, Li_2S_2 and Li_2S anchored on Ti_2NO_2, it has been confirmed that the metallic character of Ti_2NO_2 and Ti_2NF_2 could be preserved after adsorption of these sulfur-related species. In this sense, the trapped LiPS species could be easily reduced, which supplies their own free electrons to support the redox reaction of sulfur species. Similar observations were also disclosed in F- and O-functionalized Ti_2C (Ti_2CF_2 and Ti_2CO_2).[33] Hence, Ti_2NO_2, Ti_2NF_2, Ti_2CF_2 and Ti_2CO_2 hold great promise for Li–S batteries with enhanced

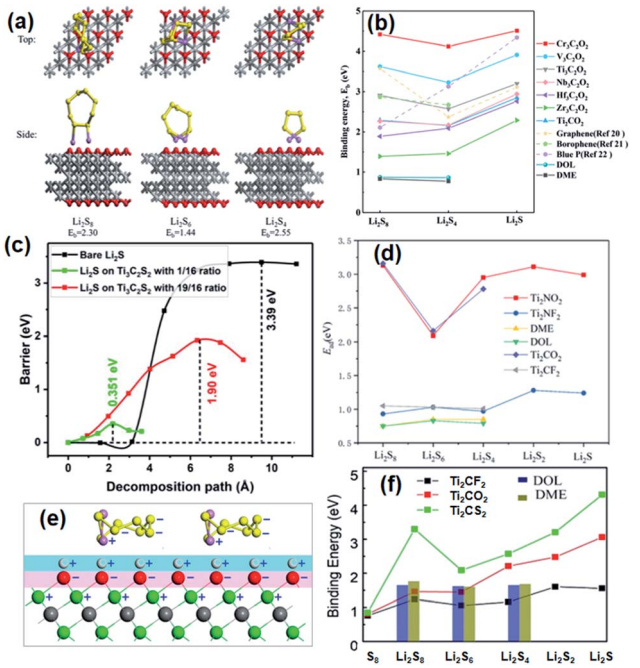

Fig. 5 (a) The optimized structures of Li_2S_8, Li_2S_6 and Li_2S_4 adsorbed on the $Ti_3C_2O_2$ monolayer and the corresponding binding energies. Reproduced with permission.[29] Copyright 2017, Elsevier. (b) Plots of the calculated binding energies between LiPS and various $M_3C_2O_2$ MXenes. Reproduced with permission.[30] Copyright 2019, Royal Society of Chemistry. (c) Decomposition barriers of bare Li_2S (black) and Li_2S on the $Ti_3C_2S_2$ supercell with Li_2S to $Ti_3C_2S_2$ ratios of 1/16 (green) and 19/16 (red). Copyright 2019, American Chemical Society.[31] (d) Adsorption energies between various substrates and Li_2S_x species. Reproduced with permission.[32] Copyright 2018, Elsevier. (e) Scheme of charged atoms in Li_2S_x and MXenes ("+" represents the electropositive atoms and "−" represents the electronegative atoms). Ti: green balls; S: yellow balls; Li: purple balls; O or F: red balls in the pink area; and H: white balls in the light-blue area. Reproduced with permission.[28] Copyright 2017, American Chemical Society. (f) Comparison of the binding energies of Li_2S_x with Ti_2CS_2, Ti_2CO_2 and Ti_2CF_2. Reproduced with permission.[34] Copyright 2018, Elsevier.

electrochemical performance. However, Rao *et al.* have also indicated that the attractions between Ti and S atoms would be undesirably weakened owing to the increased repulsive force from O- and F-termination groups to S,[28] which reasonably explains why the binding energies of LiPS on functionalized MXenes are much smaller than those on bare MXenes; the binding energies follow the order Ti_2CF_2 < Ti_2CO_2 < $Ti_2C(OH)_2$. Strikingly, the undesired repulsive force is slightly shielded by the injection of H atoms since the positively charged H atoms increase the attraction to S atoms, as schematically depicted in Fig. 5c. Moreover, the theoretical calculation results show that–O groups increase while –OH groups decrease after coming into contact with long-chain LiPS since the protruding H atoms on the MXene surface are relatively easily replaced by Li due to the lower dissociation energy of H leaving from the MXene than–OH groups. As such, the electronic conductivity of MXenes is scarcely affected by LiPS adsorption as the band gaps have no obvious change. Similarly, surface-sulfuretted Ti_2C (Ti_2CS_2) MXenes have also been investigated (Fig. 5d).[34] Compared with Ti_2CO_2 and Ti_2CF_2 MXenes, Ti_2CS_2 has the strongest affinity to LiPS; their binding energies follow the order Ti_2CF_2 < Ti_2CO_2 < Ti_2CS_2. Li prefers to interact with the sites around negatively charged atoms, such as O and F, while it repels positively charged Ti atoms. S-terminated MXenes may intrinsically balance the affinity force and repulsive force between the corresponding interacting pairs (F–Li and F–Ti) due to the lowest electronegativity of S (S: 2.58, O: 3.44 and F: 3.98). Obviously, this statement to some extent supports Rao's report.[28] S-terminated MXenes have yet not been experimentally realized, but strong affinity toward polysulfides could suppress the shuttle effect of LiPS; the metallic character and low energy barrier for Li diffusion on the surface are favorable for facilitating the electrochemical reaction of sulfur species. These advantages of S-terminated MXenes shed light on the design of sulfur host materials for high performance Li–S batteries.

3.2 Non-uniformly functionalized MXenes

The theoretical model of MXenes in DFT calculations is an assumed ideal structure, where its surface is uniformly terminated with one kind of functional group. Nevertheless, the surface of MXenes is not uniform as an ideal structure, and is almost impossible to terminate with one specific functional group alone. It has been consistently reported that MXenes have complicated surface terminations based on the experimental results.[22] Therefore, it is necessary to investigate the interactions between the non-uniformly functionalized surface of MXenes and LiPS to optimize MXenes as efficient AMs for Li–S batteries. Chung and co-works have investigated the anchoring effects of LiPS on both F- and O-functionalized Ti_2C MXenes using a spin-polarized DFT calculation model,[35] in which the substitutional, vacancy and S-trapped sites of F- and O-functionalized Ti_2C are collectively discussed (Fig. 6). The F-substitutional sites on the Ti_2CO_2 surface prevent the neutralization of S atoms through weakening of the interactions between Li and O atoms, and the suppressing mechanism is changed depending on the existence of the –F functional group despite the adsorption of LiPS on the Ti_2CO_2 surface. However, O-substitutional sites induce stronger interactions with Li atoms than dominant F sites, and they are preferentially favored in terms of energetics to anchor LiPS. It has also concluded that the surface vacancy sites (the surface partially uncovered with –F or –O groups) result in the stabilization of S atoms with a possible loss of active materials because strong interactions between exposed Ti and S atoms break the S–S covalent bonds in sulfur species. Thus, the preparation process of MXenes should be focused on decreasing the vacancy of the functional groups as much as possible rather than pursuing surface functionalization with one type of specific functional group.

The large-scale application of Li–S batteries could not be realized unless the challenge of dissolution of soluble LiPS species in electrolytes is solved. Although some of the theoretical statements for the anchoring effects of LiPS on MXenes may be hard to realize due to the gap between theoretical and experimental observations, these theoretical studies have provided insight into the modeling of MXenes and more intuitive information to optimize MXenes as the AM for high-performance Li–S batteries.

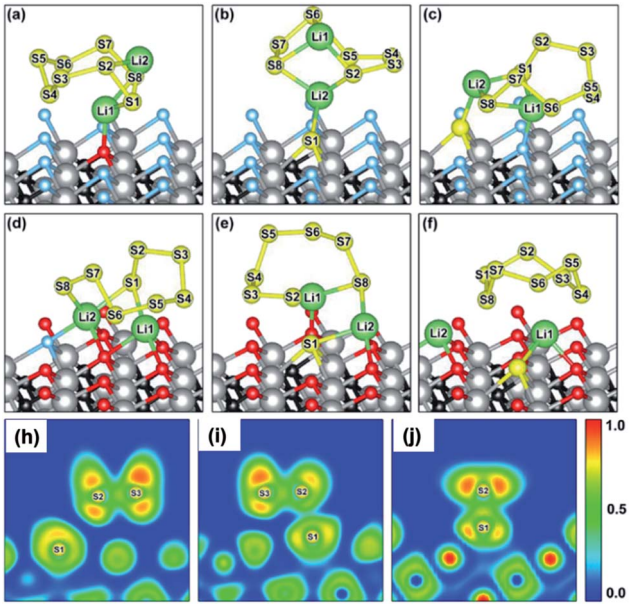

Fig. 6 Optimized configurations of Li_2S_8 anchored on the (a) substitutional, (b) vacancy and (c) S-trapped sites of F-functionalized Ti_2C and on the (d) substitutional, (e) vacancy and (f) S-trapped sites of O-functionalized Ti_2C. The gray, black, sky blue, red, yellow and green spheres represent Ti, C, F, O, S and Li atoms, respectively. Electron localization functions of Li_2S_8 on the vacancy sites of (g) F-functionalized and (h) O-functionalized Ti_2C, and (i) isolated Li atom on the S-trapped site of F-functionalized Ti_2C. The localized electron density was normalized from 0 to 1. Reproduced with permission.[35] Copyright 2018, Elsevier.

4. Experimental advances of MXene-based Li–S batteries

The use of MXenes in the cathodes, anodes and interlayers/hybrid separators as well as the relationship between their intrinsic properties and electrochemical performance are described in this sub-section. The related performance parameters for the reported MXenes-engineered Li–S batteries are summarized in Table 1.

4.1 MXene-engineered sulfur cathodes

Beyond the conventional encapsulation of active sulfur into porous carbonaceous matrixes,[8,36–39] an avalanche of research studies has recently been published to address the shuttle effects of LiPS by using various polar nanostructured materials with specific chemisorption and electrochemical kinetic manipulation to LiPS.[17–19] Thereinto, MXenes with high conductivity and rich surface terminations are promising hosts to immobilize LiPS within the cathode.[22] According to the constituents in the MXene–hybridized sulfur composites, they are classified as MXene–S binary hybrids, MXene–C/S ternary hybrids and MXene–AM/S ternary hybrids.

4.1.1 MXene–S binary hybrids. Nazar and co-work have pioneered the direct use of Ti_2CT_x MXenes in Li–S batteries and predicted the effectiveness of other MXene phases as sulfur hosts for high-performance Li–S batteries.[27,40] It should be mentioned that the specific surface area of the as-prepared Ti_2CT_x MXene is only about 68 $m^2\ g^{-1}$, which is far less than that in traditional porous carbonaceous hosts. Notwithstanding, the Ti_2CT_x–S binary composite has exhibited long-term cycling performance with a discharge capacity of 723 mA h g^{-1} after 650 cycles at 0.5C. The superior performance is attributed to the chemisorption of LiPS on the Ti_2CT_x surface and the formation of S–Ti–C bonds promotes the electron transfer and reaction kinetics of LiPS. By thermal annealing of negatively charged $Ti_3C_2T_x$ MXene flakes and positively charged melamine, Wang and co-workers have prepared crumpled nitrogen-doped MXene nanosheets with a high specific surface area of 385 $m^2\ g^{-1}$ and a pore volume of 0.342 $cm^3\ g^{-1}$ (Fig. 7a–h) and strong physical and chemical dual-adsorption for LiPS have been displayed.[41] This binary $Ti_3C_2T_x$–S composite achieves an areal sulfur loading of 5.1 mg cm^{-2} and outstanding electrochemical performance, including a high reversible capacity of 1144 mA h g^{-1} at 0.2C, a high level of capacity retention of 950 mA h g^{-1} after 200 cycles and an extended cycling stability of 610 mA h g^{-1} at 2C after 1000 cycles. Besides conventional slurry coating-derived cathodes, freestanding MXene–S cathodes were also reported as well. Yang and co-workers have used viscous aqueous ink of nanoscale sulfur and $Ti_3C_2T_x$ nanosheets to fabricate freestanding and flexible $Ti_3C_2T_x$/S electrodes.[42] They have proposed that soluble LiPS is efficiently chemisorbed and converted into thiosulfate and a subsequent sulfate complex. The *in situ* formed sulfate complex layer acts as a protective barrier for suppressing the migration of LiPS, leading to the enhancement of S utilization and cycling stability. Wang and co-workers have fabricated a self-supporting $Ti_3C_2T_x$ foam/S cathode through a hydrazine-induced foaming technique and subsequent physical infiltration of sulfur.[43] In virtue of good electrolyte wettability and structural stability, the resultant self-supporting electrode achieves a high initial discharge capacity of 1226.4 mA h g^{-1} at 0.2C, a rate performance of 711.0 mA h g^{-1} at 5C and an extended cycling stability of 689.7 mA h g^{-1} after 1000 cycles with a sulfur loading of 5.1 mg cm^{-2}. Moreover, a gravimetric energy density of 1297.8 W h kg^{-1} is acquired. More recently, freestanding and flexible $Ti_3C_2T_x$/S conductive paper was reported to combine superior electrical conductivity, mechanical strength and strong chemisorption of LiPS (Fig. 7i–l). Based on these advantages, the as-prepared $Ti_3C_2T_x$/S electrode delivers high initial discharge capacity and an ultralow capacity decay rate of 0.014% over 1500 cycles, recording the lowest value reported for MXene-based Li–S batteries to date.[44] Besides, Pourali and co-workers have recently reported a $Ti_3C_2T_x/Li_2S$ nanocomposite.[45] Benefiting from the lower Li^+ transport energy barrier through nano-sized Li_2S particles and homogeneous distribution of solid sulfur particles, the as-prepared electrode has exhibited superior electrochemical performance when compared with the commercial Li_2S counterpart.

In light of the fabrication of high-energy-density Li–S batteries, the use of the low tap density of sulfur host materials inevitably results in a low volumetric capacity when the areal sulfur loading is increased in order to achieve a high areal capacity, which greatly compromises their application in

Table 1 A summary of the related performance parameters for reported MXene-based Li–S batteries

Material samples	Category	Areal sulfur loading (mg cm^{-2})	Rate	Cycle number	Capacity (mA h g^{-1})	Promoted mechanism	Ref
Ti_2C–S	Cathode	1	0.5C	400	960	Chemical adsorption	28
S/CNT–Ti_3C_2	Cathode	1.5	0.5C	1200	450	"Double mechanism"	40
		5.5	0.2C	250	450		
N–$Ti_3C_2T_x$/S	Cathode	1.5	0.2C	200	950	Chemical adsorption	41
		5.1	0.2C	500	588		
S@$Ti_3C_2T_x$	Cathode	~2.5	0.2C	800	724	"Double mechanism"	42
$Ti_3C_2T_x$/S	Cathode	1.5	1C	1000	689.7	Chemical adsorption	43
$Ti_3C_2T_x$/S paper	Cathode	1.0	1C	1500	970	Chemical adsorption	44
Li_2S/$Ti_3C_2T_x$	Cathode	1.6	0.1C	100	528	Chemical adsorption	45
Flower-like $Ti_3C_2T_x$–S	Cathode	10.5	0.033C	10.04	746	Electrocatalysis	47
$Ti_3C_2T_x$@meso-C/S	Cathode	2	0.5C	300	704.6	Chemical adsorption	50
$Ti_3C_2T_x$/RGO/S	Cathode	1.5	0.5C	300	878.4	Chemical adsorption	51
$Ti_3C_2T_x$/rGO/S	Cathode	1.57	1C	500	596	Chemical adsorption	52
		6	0.1C	30	879		
Ti_3C_2/S@PDA	Cathode	1.5	0.5C	200	1096	Dual-chemisorption	53
		5	0.2C	1000	651		
S@Ti_3C_2@PDA	Cathode	1	0.2C	150	1044	Dual-chemisorption	54
		4.4	0.5C	330	556		
TiO_2 QDs@Ti_3C_2/S	Cathode	1.5	2C	500	680	Chemical adsorption	56
		5.5	0.2C	100	309		
TiO_2–$Ti_3C_2O_x$–S	Cathode	Unknown	1C	1000	662	Chemical adsorption	57
S@TiO_2/Ti_2C	Cathode	1.8–2	2C	200	464	Chemical adsorption	58
			5C	200	227.3		
Ti_3C_2/1T–2H MoS_2–C–S	Cathode	2–4	0.5C	300	799.3	Electrocatalysis	59
Ti_3C_2 nanodot/nanosheet	Cathode	1.8	2C	400	815	Electrocatalysis	61
		13.8	0.1C	50	550		
Ti_3C_2–Li	Anode	Unknown	—	—	—	Lithiophobicity	66
Ti_3C_2@CP	Separator	2.6	5 mA cm^{-2}	500	980	Dual-chemisorption	
$Ti_3C_2T_x$ nanosheet	Separator	1.2	0.5C	500	550	Chemical adsorption	74
Ti_3C_2 nanosheet/glass fiber	Separator	1.9	0.5 A g^{-1}	100	721	Chemical adsorption	75
Ti_3C_2 debris eggshell membrane	Separator	2.07	0.5C	250	447	Chemical adsorption	76
Ti_3C_2 nanoribbon/nanosheet	Cathode + separator	0.7–1	0.5C	200	~400	Chemical adsorption	78
$Ti_3C_2T_x$–PEI–CNT	Cathode + separator	2.6	0.25C	200	~1100	Chemical adsorption	79
TiO_2–$Ti_3C_2T_x$ heterostructures	Separator	1.2	2C	1000	~600	Electrocatalysis	80
$Ti_3C_2T_x$–PP	Separator	1.2	1C	200	640	Chemical adsorption	81

compact areas imposed by device volume and chip area.[46] Carbon-based materials usually possess a low tap density; the elimination of conductive carbon materials in binary MXene–S composites enables high volumetric capacity owing to the high tap density of MXenes. Very recently, our research group has proposed the concept of carbon-free Li–S batteries based on flower-like porous $Ti_3C_2T_x$ (FLPT) for synchronous gain in high areal and volumetric capacities (Fig. 7m and n).[47] In this case, no conductive carbon matrix is applied in the $Ti_3C_2T_x$–S composites and no extra carbon additives are incorporated during slurry coating. The micron-sized FLPT assemblies enable the space-efficient arrangement of primary $Ti_3C_2T_x$ nanosheets and thus result in a high tap density (3.13 g cm^{-3}) in the FLPT–S composite. The resultant FLPT–S electrode simultaneously acquires a high areal capacity of 10.04 mA h cm^{-2} and an ultrahigh volumetric capacity of 2009 mA h cm^{-3}, realizing a synchronous gain in high areal and volumetric capacities (Fig. 7o). As an exhilarating discovery, a dynamic equilibrium between the S_6^{2-} anion and S_3^{*-} radical during cycling was confirmed in this engineered MXene–S system (Fig. 7m). However, the dynamic equilibrium between S_6^{2-} species and S_3^{*-} radicals is relatively sluggish in conventional carbon-based systems, as evidenced by a combination of UV-vis and electron paramagnetic resonance (EPR) techniques (Fig. 7m). Generally, the S_3^{*-} radical-facilitated mechanism is hard to disclose in conventional carbon-based systems since the sp^2 carbon signal in EPR almost overlaps with that of S_3^{*-} radicals,[48] although post-treatments of the collected data could alleviate the interference from the sp^2 carbon signal to some extent,[49] while this dilemma could be efficiently settled in a carbon-free $Ti_3C_2T_x$–S system. The possible synergistic effect between carbon and $Ti_3C_2T_x$ is excluded owing to the absence of conductive carbon, enabling more convincing results for mechanism investigation. The MXene–S systems without conductive carbon additives provide new platforms for the investigation of the electrochemical mechanism and temporal speciation in Li–S batteries.

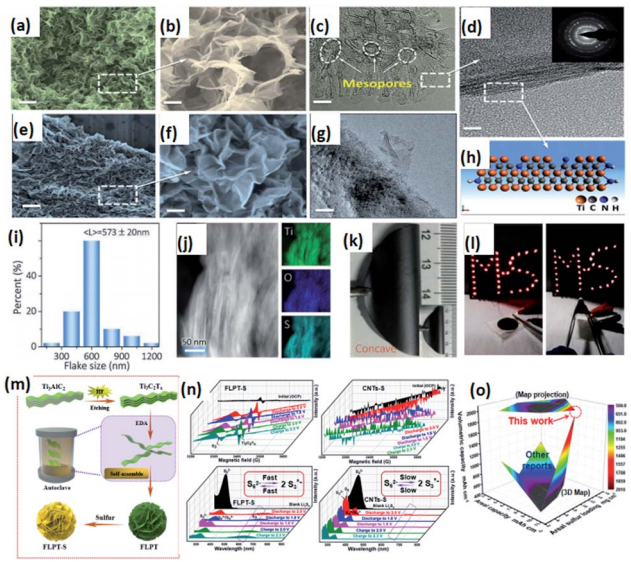

Fig. 7 (a and b) SEM image of crumpled N–$Ti_3C_2T_x$ nanosheets. (c and d) HRTEM image and SAED pattern of crumpled N–$Ti_3C_2T_x$ nanosheets. (e and f) FESEM image of crumpled N–$Ti_3C_2T_x$/S composites. (g) HRTEM image of crumpled N–$Ti_3C_2T_x$/S composites. (h) Schematic diagram of crumpled the N–$Ti_3C_2T_x$ monolayer. Reproduced with permission.[42] Copyright 2018, WILEY-VCH. (i) The lateral size distribution of the delaminated $Ti_3C_2T_x$ flakes. (j) TEM images of $Ti_3C_2T_x$/S paper and the corresponding EDX elemental mapping of Ti, O and S. (k) Photographs of freestanding $Ti_3C_2T_x$/S paper. (l) Application of the pouch cells by lighting an "M-S"-shaped string containing 37 LEDs at flat (left) and bent (right) states. Copyright 2019, WILEY-VCH.[44] (m) Schematic illustration of the synthesis of FLPT. (n) *Ex situ* EPR spectra and UV-visible absorption spectra of FLPT–S and CNTs–S electrodes at different charge/discharge states. (o) 3D projection map of areal sulfur loading *vs.* areal capacity *vs.* volumetric capacity. Reproduced with permission.[47] Copyright 2019, American Chemical Society.

4.1.2 MXene–C/S ternary hybrids. Great expectations are placed on MXenes to compete with graphene in versatile applications of 2D materials. Quite similar to graphene, one insurmountable barrier faced by delaminated MXenes is their strong tendency to restack due to interlayer hydrogen bonds and van der Waals interactions,[22] which leads to substantial loss of the specific surface area and inaccessibility of the active sites. However, carbon materials could exert their virtues of light weight, high surface area and large pore volume for accommodating solid charge/discharge products of S/Li_2S, although they are unfavorable for the adsorption and conversion of LiPS species. The hybridization of MXenes with conductive carbon materials is one of the effective solutions. Wang and co-workers have synthesized a $Ti_3C_2T_x$@mesoporous carbon architecture using metal organic frameworks as the carbon precursor.[50] The incorporated mesoporous carbon with a robust and hierarchical porous structure provides sufficient space for confining active materials and cushioning volumetric expansion of the sulfur cathode during cycling. The resultant ternary MXene–C/S cathodes achieved a high discharge capacity of 1225.8 mA h g^{-1} and more than 300 cycles at 0.5C. Nazar and coworkers have incorporated carbon nanotubes (CNTs) into the MXene phase for improving the conductivity and preventing restacking of the delaminated MXene nanosheets, which endow the resultant electrodes with excellent long-term cycling performance and fading rates as low as 0.043% per cycle for up to 1200 cycles.

Aiming at maximum utilization of the abundant functional surface of 2D exfoliated MXenes, reduced graphene oxides (rGO) nanosheets were also employed as interlayer spacers to construct a 3D sandwich-like structure with affluent accessible 2D surfaces (Fig. 8a–c),[51] in which the unique hydrophilic surface of MXene nanosheets could effectively entrap LiPS and extend the lifespan of Li–S batteries. Cooperatively, rGO is able to ameliorate the re-stacking of MXene nanosheets, making the best use of the available MXene nanosheets. The ternary sulfur composite delivers a higher capacity, better rate performance and more cycling stability than the binary rGO–S counterpart. As an extended development, Wang and co-works have developed a self-supporting $Ti_3C_2T_x$/rGO hybrid aerogel electrode using a liquid Li_2S_6 catholyte as the active material (Fig. 8d).[52] Different from solid sulfur precursors, the Li_2S_6-based cathode contributes to homogeneous distribution of active materials within the conductive backbone. The robust aerogel electrode under a high areal sulfur loading of 6 mg cm^{-2} delivers a high capacity of 1270 mA h g^{-1} at 0.1C and good cycling stability at 1C for 500 cycles with a low capacity decay rate of 0.07% per cycle. The facile integration strategy for $Ti_3C_2T_x$ and conductive carbon materials could be extended to couple other MXenes and advanced materials for widespread application in high-performance Li–S batteries.

4.1.3 MXene–AM/S ternary hybrids. Fabricating sulfur/carbon composite cathodes with sulfur confined in nanostructured carbon materials has captured considerable interest. However, conductive carbons as sulfur hosts have congenital

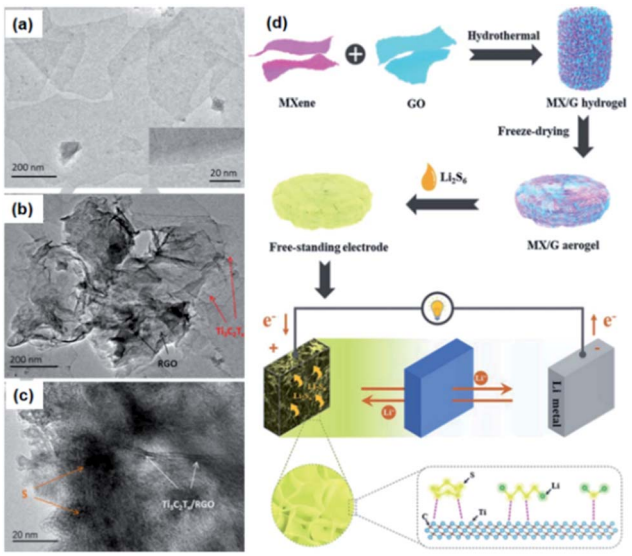

Fig. 8 (a) TEM image of ultrathin $Ti_3C_2T_x$ MXene nanosheets. (b) TEM images of hybrid $Ti_3C_2T_x$/rGO nanosheets and (c) $Ti_3C_2T_x$/rGO/S composites. Reproduced with permission.[51] Copyright 2017, Wiley-VCH. (d) The schematic illustration of the preparation of the MX/G aerogel electrode and Li–S cell assembly. Reproduced with permission.[52] Copyright 2019, Royal Society of Chemistry.

deficiencies, such as low tap density and weak LiPS chemisorption. Hence, hybridizing MXenes with carbon materials inevitably dilutes the overall polar active sites within the whole cathode composites and leads to high cell volume. Recently, some polar materials, such as transition metal oxides, sulfides and polymers, have been harnessed as the mediators of MXenes for improving the entrapment ability of LiPS and/or exerting positive kinetic effects on the conversion of LiPS,[17–19] which promotes the fabrication of MXene-based sulfur cathodes with improved discharge capacities and cycling performance. Three types of mediators including polymers, metal oxides and isogenous MXenes for ternary sulfur cathodes are described in this sub-section.

4.1.3.1 MXene–polymer/S ternary hybrids. A fly in the ointment of 2D materials is that their open access may hinder their widespread application in specific occasions in Li–S batteries, where the generated LiPS easily dissolve into the electrolytes. Although the dissolution of LiPS could be alleviated by the strong polar surface of MXenes to some extent, the tendency of LiPS dissolution into the electrolytes is intensified with their accumulated adsorbing on the outer surface, which inevitably results in final leakage of active materials when the adsorption capability between MXene and outermost LiPS is insufficient to retard the solvation behavior of LiPS in organic electrolytes. In this sense, a dual polysulfide confinement strategy has been recently proposed by Yang and co-workers,[53] where sulfur is embedded into the layer space of $Ti_3C_2T_x$ and further wrapped by a thin layer of polydopamine (PDA), as shown in Fig. 9a. $Ti_3C_2T_x$ acts as a highly conductive skeleton and active 2D surface to chemically bond with LiPS and the coated PDA layer could not only prevent sulfur from direct contact with the liquid electrolyte, but also physically and chemically strap sulfur species in the MXene nanosheets, as proved by XPS measurements (Fig. 9b). Moreover, the coated PDA sheath is substantially favorable for mechanical flexibility of the ternary composite, which maintains the structural integrity of cathode during charge/discharge. This dual LiPS immobilization mechanism based on the $Ti_3C_2T_x$ MXene matrix and PDA coating layer guarantees high electrochemical performance under a high sulfur loading of 5 mg cm^{-2}, and the ternary sulfur electrode delivers an initial discharge capacity of 1001 mA h g^{-1} with a capacity retention of 65% over 1000 cycles at 0.2C (Fig. 9c). A similar scenario with prominent electrochemical performances was also witnessed (Fig. 9d–h).[54] However, the PDA coating strategy is processed in Tris-buffer aqueous solution with intensive mechanical stirring overnight, and the active sulfur in the MXene–S precursor may undergo arbitrary loss and the sulfur content in the final ternary composite is hard to control. Moreover, the excess coating of PDA largely decreases the overall sulfur content in the composites, thus compromising the energy density of Li–S batteries. Designing an easy-to-operate coating strategy on the MXene–S composite is highly desirable to shed light on their prospects as advanced cathode materials.

4.1.3.2 MXene–metal oxides/S ternary hybrids. Metal oxides are among the first group of AMs that have been extensively employed to stabilize soluble LiPS, which curtails the inexorable

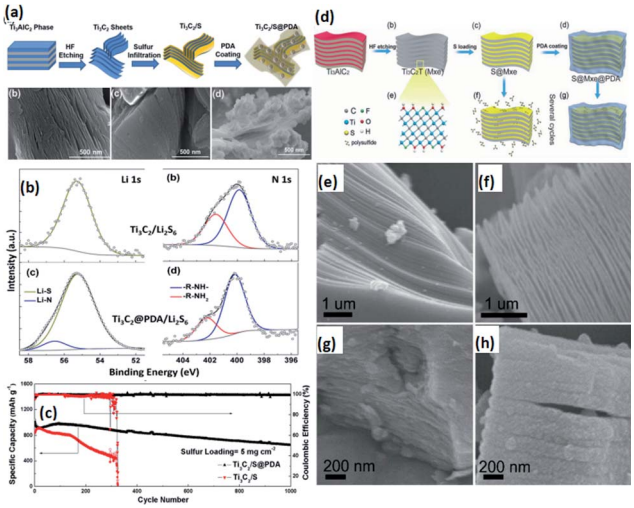

Fig. 9 (a) Schematic illustration of the fabrication of the $Ti_3C_2T_x$/S@PDA composite and the corresponding SEM images of $Ti_3C_2T_x$ sheets, $Ti_3C_2T_x$/S and $Ti_3C_2T_x$/S@PDA composites. (b) XPS analyses to show the interaction between the $Ti_3C_2T_x$ host and Li_2S_x. (c) $Ti_3C_2T_x$/S and $Ti_3C_2T_x$/S@PDA cathodes with a sulfur loading of 5.0 mg cm^{-2} at 0.2C. Reproduced with permission.[54] Copyright 2018, Wiley-VCH. (d) Synthetic procedure of the S@MXene@PDA electrode and illustration of LiPS migration from the S@MXene cathode after several cycles. SEM images of (e) Ti_3AlC_2 phase, (f) MXene, (g) S@MXene and (h) S@MXene@PDA. Reproduced with permission.[53] Copyright 2019, Elsevier.

leakage of active materials into the electrolytes.[55] The difference in electronegativity between oxygen atoms and transition metal atoms induces high surface polarity in metal oxides, which serve as sulfur hosts to effectively interact with polar LiPS. Gao and co-workers have selected metal oxide quantum dots as mediators for improving the electrochemical performance of MXene-based Li–S batteries;[56] TiO_2 quantum dots (QDs) were grown on ultrathin $Ti_3C_2T_x$ MXene nanosheets through cetyltrimethylammonium bromide (CTAB)-assisted solvothermal synthesis (Fig. 10a). The attached TiO_2 QDs not only introduce extra active sites for LiPS entrapment, but also serve as spacers to isolate the MXene nanosheets from restacking, which guarantees a larger accessible electrode–electrolyte contact area (Fig. 10b).As a result, the engineered hybrid cathode exhibits substantially promoted cycling stability and rate capability. Similarly, an accordion-like TiO_2–$Ti_3C_2T_x$ MXene heterostructure was synthesized through fast annealing treatment of $Ti_3C_2T_x$ MXene in air.[57] In this scenario, the dominant surface termination on the $Ti_3C_2T_x$ MXene after heat treatment is O, which contributes to extra lithium storage to the sulfur cathode, resulting in a reversible capacity of 367 mA h g^{-1} at a high rate of 10C, including the contribution from $Ti_3C_2T_x$ itself. These results suggest that the variation in terminal groups on the MXene surface may alter the lithium storage mechanism at the C–Ti interface. Recently, a TiO_2 hollow nanosphere embedded Ti_2C MXene was reported as a sulfur host as well.[58] The S@TiO_2/Ti_2C ternary electrode exhibits a large initial discharge capacity of *ca.* 1408.6 mA h g^{-1} at 0.2C under a sulfur content of 78.4 wt% and a sulfur loading of about 2.0 mg cm^{-2}. The electrode still maintains reversible capacities of up to 464.0 and 227.3 mA

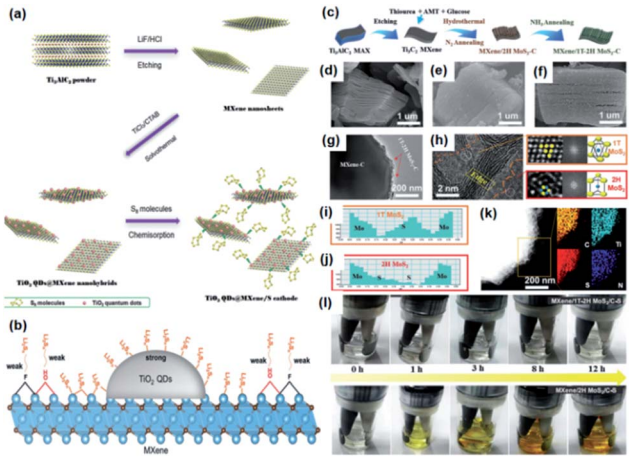

Fig. 10 (a) Schematic illustration of the preparation of $Ti_3C_2T_x$ nanosheets from Ti_3AlC_2 by LiF/HCl etching, the growth of TiO_2 QDs on MXene nanosheets by CTAB-assisted solvothermal synthesis as well as the fabrication of the TiO_2 QDs@MXene/S cathode by chemisorption of S8 molecules. (b) TEM image of TiO_2 QDs@MXene nanohybrids. (c) EDS maps of TiO_2 QDs@MXene/S. Reproduced with permission.[56] Copyright 2018, Wiley-VCH. (c) Schematic illustration of the fabrication of MXene/1T–2H MoS_2–C composites. SEM images of (d) MXene, (e) MXene/2H MoS_2–C and (f) MXene/1T–2H MoS_2–C. (g) TEM and (h) HRTEM images of MXene/1T–2H MoS_2–C. (i and j) The intensity profile along the lines taken from (h). (k) Elemental mapping images of MXene/1T–2H MoS_2–C. (l) Digital photos of glass vials with the MXene/1T–2H MoS_2–C–S and MXene/2H MoS_2–C–S batteries as discharge time increases. Reproduced with permission.[59] Copyright 2018, Wiley-VCH.

h g^{-1} after 200 cycles at high current rates of 2C and 5C, respectively. More recently, the phase engineering strategy has been demonstrated using MXene/1T–2H MoS_2–C for boosting the performance of Li–S batteries (Fig. 10c–l).[59] High-resolution TEM images and EPR measurements show that positively charged S-vacancy defects are *in situ* formed on MXene/1T–2H MoS_2–C (Fig. 10h), which serve as strong adsorption and activation sites for polar LiPS. Taking advantage of defect engineering, the MXene/1T–2H MoS_2–C–S cathode exhibits a high initial capacity of 1194.7 mA h g^{-1} at 0.1C and a high capacity retention of 799.3 mA h g^{-1} over 300 cycles at 0.5C. However, the incorporation of TiO_2 and MoS_2 is a double-edged sword; the content of TiO_2 or MoS_2 on the MXene surface should be carefully tailored, otherwise the overall conductivity of the ternary composites will be compromised owing to the insulating feature of TiO_2 and MoS_2 with inferior Li-ion diffusivity ($\sim 10^{-12}$ to 10^{-9} cm^2 s^{-1}) and electric conductivity ($\sim 10^{-12}$ to 10^{-7} S cm^{-1}). Whether employed as sulfur hosts or utilized as additives in Li–S batteries, the MXene-based materials should be further studied to experimentally verify the interactions of LiPS on surface-functionalized MXenes with various terminations.

4.1.3.3 MXene–MXene/S ternary hybrids. For practical application of sulfur electrodes, the areal capacity of Li–S batteries should be 4 mA h cm^{-2} in order to be comparable with state-of-the-art commercial LIBs.[60] The average voltage of traditional lithium intercalated metal oxide-based LIBs is about 3.5 V, while it is only about 2.1 V in Li–S batteries. After an approximate mathematic transformation, the areal capacity of Li–S batteries should be 6.7 mA h cm^{-2} to match the energy requirements for transportation. Accordingly, sulfur loading needs to reach at least 5.6 mg cm^{-2} to meet these goals, assuming that the practical discharge capacity of sulfur is up to 1200 mA h g^{-1}. Unfortunately, the majority of the reported data based on MXene-engineered ternary sulfur cathodes resides far below the discussed sulfur loading level and areal capacity. To this end, our research group has recently reported a $Ti_3C_2T_x$ MXene nanodot-interspersed $Ti_3C_2T_x$ nanosheet (TCD-TCS) as the sulfur host material (Fig. 11a and b).[61] In such a well-designed MXene architecture, the intimate connection between isogenous nanodots and nanosheets could greatly decrease their interfacial resistance, thus expediting global electron transport and electrochemical reaction kinetics. The high density of surface polar sites could not only minimize the dissolution and shuttle effect of LiPS, but also mediate the deposition of solid discharge products, thus enabling high sulfur utilization even under high current densities and high sulfur loading. An almost theoretical discharge behavior is achieved with a medium areal sulfur loading of 1.8 mg cm^{-2} at 0.05C (Fig. 11c and d). Owing to the absence of the carbon matrixes and conductive additives, the MXene/MXene–S cathode exhibits ultrahigh volumetric capacity (1957 mA h cm^{-3}) and high areal capacity (13.7 mA h cm^{-2}) under a high areal sulfur loading of 13.8 mg cm^{-2}. Unfortunately, the electrode could only be stably operated for 50 cycles. The low stability is attributed to the fact that a high areal current is apportioned on the lithium anode at such high sulfur loading, which aggravates dendrite formation and impedance build-up on the anode surface, thus giving rise to electrolyte depletion and voltage fluctuations. The lithium anode corrosion may turn into a dominating factor in limiting the performance of high-sulfur-loaded MXene cathodes. An engineered lithium metal anode that is dendrite-free at high current density and high sulfur loading is required to achieve high-performance Li–S batteries.

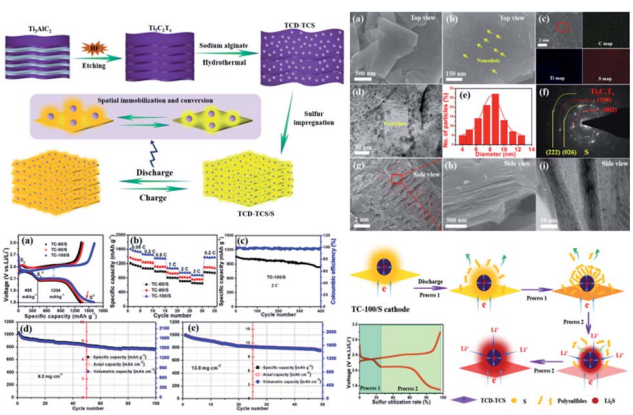

Fig. 11 (a) Schematic illustration of the preparation of TCD-TCS and TCD-TCS/S. (b) Morphological characterization of the TCD-TCS/S composite. (c) Electrochemical performances of the TCD-TCS/S cathode. (d) Schematic illustration of the evolution of active materials during the discharge process for TCD-TCS/S cathodes. Reproduced with permission.[61] Copyright 2019, American Chemical Society.

The above studies show that almost all MXene-engineered cathode systems are based on the $Ti_3C_2T_x$ MXene, which is probably attributed to its high electrical conductivity and relatively facile synthesis process when compared with other MXenes. It should be mentioned that apart from the "double mechanism" (*viz.* Lewis acid–base interaction and thiosulfate/polythionate conversion), the promoted electrochemical performance of the MXene-engineered sulfur electrode is generally attributed to chemical adsorption capability and electrocatalytic behavior of $Ti_3C_2T_x$ for LiPS, as categorized in Table 1.

4.2 MXene-engineered anodes

Metallic lithium has been deemed as an optimal anode material for advanced Li-based batteries owing to its high theoretical capacity of 3860 mA h g^{-1} and the lowest potential of −3.04 V *vs.* the standard hydrogen electrode and because of it having the lightest weight among metals.[62] Aiming at avoiding the formation of dangerous dendritic lithium on its surface and the pulverization of dense Li metal during cycling, recent investigations are rejuvenating Li-metal anodes for Li-metal batteries.[63–65] Nevertheless, the findings based on Li/Li symmetrical cells may not be directly applicable in Li–S batteries. The issues of Li are largely exaggerated since the dissolved LiPS participates in the formation of unstable solid electrolyte interphase (SEI) layers on the Li metal anode. Inspired by the proposed lithiophilic hosts,[66] a $Ti_3C_2T_x$ MXene–Li film was fabricated based on the unique malleability of metallic Li and lubricity of atomic layers through a roll-to-roll mechanical approach (Fig. 12).[67] In this hybrid Li film, high interlayer space results in Li deposition into the gaps of $Ti_3C_2T_x$ nanosheets, which act as the SEI films for metallic Li and could be well maintained during repeated Li stripping/deposition. Meanwhile, the conductive $Ti_3C_2T_x$ allows for controllable growth of lithium dendrites in the nanoscale gaps and prevents their vertical growth to pierce the separator. The optimal film anode exhibits a low overpotential of 32 mV at 1.0 mA cm^{-2}, flat voltage profiles, high rate performance and good cycling stability. The application of MXenes in Li anodes is still at an early stage, and the progress on multifarious nanostructured Li metal will facilitate the advancement of MXene-based Li–S batteries and eventually solve the safety issues of the available Li–S batteries.

4.3 MXene-engineered separators

The design of the nanostructure architectures based on various cathode components is an effective approach for facilitating the redox reactions of solid–liquid–solid transformation.[68–71] Such components, including coated separators with a carbon or polymer coating film as well as the interlayers between the cathode and separator, are based on active material reservoirs to form an up-current collector and trapping barrier to confine LiPS within the cathode region. Modification of the polymeric separators has been regarded as one of the effective strategies to hinder free migration of LiPS between the cathode and anode.[72,73] Wang and co-workers have reported a functional

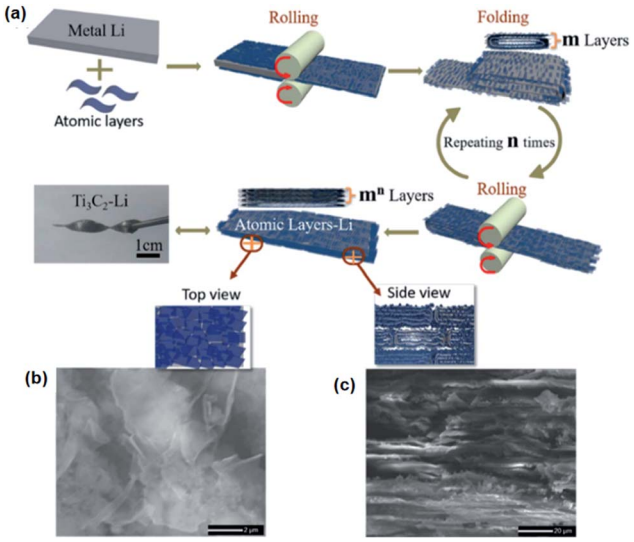

Fig. 12 (a) Schematic illustration of the synthesis of the Ti_3C_2 MXene (graphene, BN)-lithium films. (b) Top and (c) sectional SEM images of the lithiophobic layer–Li (Ti_3C_2–Li) hybrid. Reproduced with permission.[64] Copyright 2017, Elsevier.

separator for trapping LiPS by coating $Ti_3C_2T_x$ MXene nanosheets on commercial Celgard membranes *via* a facile vacuum filtering method for the first time.[74] $Ti_3C_2T_x$ forms a uniform and conformal coating layer with a mass loading of 0.1 mg cm^{-2} and a thickness of only 522 nm. Due to significantly improved electronic conductivity and trapping ability toward LiPS, the cell with a MXene-functionalized separator delivers a high discharge capacity of 550 mA h g^{-1} after 500 cycles with a capacity decay of only 0.062% per cycle at 0.5C. $Ti_3C_2T_x$ MXene nanosheet-coated glass fibers were also employed as a composite membrane for suppressing the shuttle effect of LiPS and improving sulfur utilization.[75] Recently, $Ti_3C_2T_x$ MXene debris were coated on the surface of a biodegradable eggshell membrane (ESM) to construct a functional separator MXene/ESM (Fig. 13a and b).[76] Benefiting from the high electronic conductivity and abundant surface polar groups of the MXene debris as well as good mechanical strength, superior thermal stability and large electrolyte infiltration of the ESM, the separator effectively suppresses the shuttle effect of LiPS. The electrochemical performance is greatly superior to that based on a commercial polypropylene separator. Strikingly, inspired by the all-graphene structure of a sulfur cathode prototype,[77] Wu and co-workers have designed a flexible all-MXene monolithic electrode, in which 3D alkalized $Ti_3C_2T_x$ MXene nanoribbon frameworks serve as sulfur hosts and 2D delaminated $Ti_3C_2T_x$ MXene nanosheets serve as the interlayer between the cathode and commercial separator.[78] The ingenious construction of an integrated electrode with two different MXene nanostructures completely averted the usage of an aluminum current collector, which significantly elevates the energy density to 833 W h kg^{-1}. Similarly, a ternary $Ti_3C_2T_x$–polyethyleneimine (PEI)–CNT composite was prepared by Lai and co-workers through a facile electrostatic self-assembly approach for the coupled engineering of the cathode and

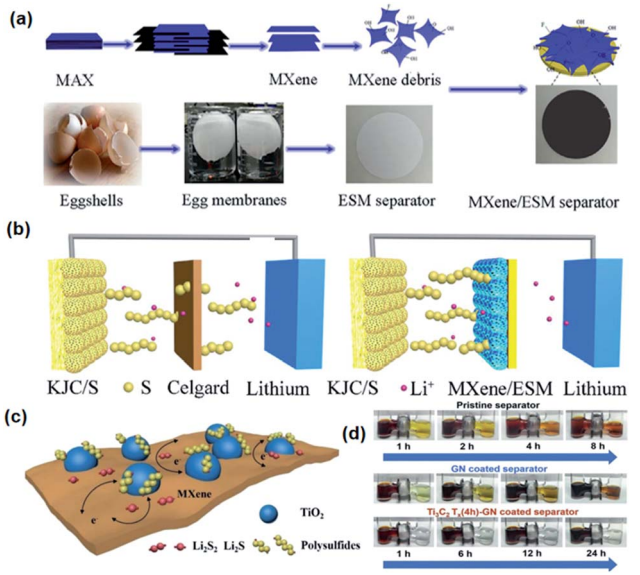

Fig. 13 (a) Schematic illustration of the preparation of MXene/ESM. (b) Schematic illustration of Li–S batteries with a Celgard separator and MXene/ESM separator. Reproduced with permission.[76] Copyright 2018, Elsevier. (c) Schematic illustration of LiPS trapping and conversion on the TiO_2–$Ti_3C_2T_x$ heterostructures. (d) Polysulfide permeation measurements with H-shaped glass cells for the pristine PP separator, GN-coated separator, and $Ti_3C_2T_x$–GN-coated separator. Reproduced with permission.[80] Copyright 2018, Wiley-VCH.

separator. The resultant cathode possesses a robust 3D heterogeneous interlinked structure, efficiently improving LiPS adsorption and interfacial redox reactions. Meanwhile, the engineered separator confers well-organized nanochannels, which enable better anti-fouling performance and high-rate cyclability.[79] More recently, taking into account the restacking feature of MXene nanosheets and negative effects of F-terminal groups on the MXene surface, $Ti_3C_2T_x$ was partially transformed into a TiO_2 phase through controlled oxidation of MXene nanosheets; the fluorine terminations on the MXene surface were largely removed and replaced by oxygen atoms to form TiO_2–MXene heterostructures.[80] The TiO_2 nanoparticles mainly serve as the active centers to trap LiPS and the hetero-interfaces promise the smooth diffusion of LiPS from TiO_2 to MXenes for further redox reaction. The assembled interlayer constructed by TiO_2–MXene and conductive graphene effectively suppresses the shuttling effect of LiPS and improves the utilization of sulfur, leading to high reversible capacity and cycling stability even under a sulfur loading as high as 7.3 mg cm^{-2}. These research advances have demonstrated the superiority of MXene nanosheets as the separator coating layers in Li–S batteries. Also, MOF-derived carbon on nitrogen-doped ultrathin $Ti_3C_2T_x$ MXenes has been reported to achieve superior electrochemical performance at a higher sulfur loading of over 10 mg cm^{-2}. Of particular note is that the thickness and weight of the coating layers on the separator need to be carefully controlled since the addition of these conductive layers inevitably increases the weight of nonactive materials in the whole cell. To this end, an ultra-lightweight CNT-bridged $Ti_3C_2T_x$/CNTs 10%-PP modified separator with an ultralow mass loading of 0.016 mg cm^{-2} was fabricated through the vacuum filtration approach,[81] which effectively inhibits LiPS shuttling and enables rapid Li^+ ion transport. Such an ultra-lightweight separator not only expands the application of MXene materials, but also potentially provides an effective approach for the development of high-performance Li–S batteries.

5. Summary and prospects

We have summarized recent theoretical and experimental progress of MXene-based materials in Li–S batteries. Their use as additives and/or conductive matrixes in cathodes, anodes and separators greatly suppresses LiPS shuttling and expedites sulfur utilization, thus leading to high discharging capacity, rate performance and cycling stability even under a high sulfur content and/or high sulfur loading. Although considerable achievements have been made in MXene-based Li–S batteries, some inherent problems still need to be solved to further improve the electrochemical performance.

(1) High polarity and rich surface chemistry of 2D MXenes are favorable for suppressing the shuttle effect of LiPS, but they are inclined to induce the restacking of MXene nanosheets through hydrogen bonding or van der Waals interactions. Hybridizing 2D MXenes and other low-dimensional nanostructures is one of the promising strategies to inhibit the restacking of MXene nanosheets, and it is of utmost significance to explore new methods and materials for their controllable integration to maximize their activity and efficiency for high-performance Li–S batteries. Moreover, in light of the respective pros and cons of conductive MXenes (strong polarity and low specific surface area) and conductive carbon materials (weak polarity and high specific surface area), appropriate hybridization of MXenes and carbon materials can achieve higher sulfur utilization especially under higher current rates.

(2) The ion dynamics and charge storage mechanism among MXene nanosheets still remain unclear. There is potential trapping of Li^+ among MXene layers even in the voltage window of 1.5–3.0 V. Capacity contribution from the MXene itself based on surface pseudocapacitance behavior or possible Li^+ intercalation behavior may exist along with the (de)lithiation of sulfur in some MXene-based sulfur cathodes. In addition, Li-uptake may result in dynamic affinities between MXene hosts and sulfur species, which exaggerates the complexity of Li–S electrochemistry. It is pivotal to explore the effects of dynamic change in interlayer spacing of these MXene hosts on the Li–S electrochemistry for developing high-performance Li–S batteries.

(3) MXenes have relatively poor oxygen resistance and are easy to oxidize due to the exposure of a large portion of metal atoms on the surface. Once overly oxidized, MXenes are inevitably distorted, and the extraordinary properties, such as metallic conductivity and chemisorption ability of LiPS, are probably impaired and even damaged. It is one of the most urgent issues to be solved to protect MXenes from oxidation during controllable synthesis, sulfur infiltration and slurry drying.

(4) Heteroatom doping is emerging as a new direction to improve the electrochemical performance of MXenes. However, performance improvement is only witnessed with N-doped $Ti_3C_2T_x$. Exploring the methods of heteroatom doping and the effects on electrochemical performance is required to enhance the electrochemical performance of MXenes in Li–S batteries.

(5) About thirty MXene compositions have currently been synthesized through top–down approaches, and more stable MXenes have been theoretically predicted. New types of MXenes are being discovered. However, this embarrassment of riches poses somewhat of a dilemma. To date, the vast majority of MXene-engineered Li–S batteries are based on $Ti_3C_2T_x$, and the composition has already shown great promise in various applications. There is no reason to believe it is the best for all scenarios. Therefore, it is urgently needed to bring our understanding of other compositions to the same level as that of $Ti_3C_2T_x$ for use in Li–S batteries.

Distinguished from well-developed carbon-based materials, the unique 2D structure, high conductivity, high polarity and rich surface chemistry of MXene materials endow them with tremendous potential for application in high-performance Li–S batteries. The advances in theoretical and experimental investigations will not only boost the development of high-energy-density Li–S batteries, but also hold great promise for potential applications in other energy storage systems.

Conflicts of interest

There are no conflicts to declare.

Acknowledgements

This work was supported by the National Natural Science Foundation of China (21601191, 21673241 and 21471151), the Natural Science Foundation of Fujian Province (2018J01030) and the Strategic Priority Research Program of the Chinese Academy of Sciences (XDB20000000).

References

1 B. Dunn, H. Kamath and J. M. Tarascon, *Science*, 2011, **334**, 928–935.
2 S. Chu and A. Majumdar, *Nature*, 2012, **488**, 294–303.
3 Y. Liu, P. He and H. Zhou, *Adv. Energy Mater.*, 2018, **8**, 1701602.
4 M. M. Thackeray, C. Wolverton and E. D. Isaacs, *Energy Environ. Sci.*, 2012, **5**, 7854–7863.
5 V. Etacheri, R. Marom, R. Elazari, G. Salitra and D. Aurbach, *Energy Environ. Sci.*, 2011, **4**, 3243–3262.
6 D. Larcher and J. Tarascon, *Nat. Chem.*, 2015, **7**, 19–29.
7 J. B. Goodenough and Y. Kim, *Chem. Mater.*, 2010, **22**, 587–603.
8 X. Ji, K. T. Lee and L. F. Nazar, *Nat. Mater.*, 2009, **8**, 500–506.
9 Z. W. Seh, Y. Sun, Q. Zhang and Y. Cui, *Chem. Soc. Rev.*, 2016, **45**, 5605–5634.
10 R. V. Salvatierra, G. A. López-Silva, A. S. Jalilov, J. Yoon, G. Wu, A. Tsai and J. M. Tour, *Adv. Mater.*, 2018, **30**, 1803869.
11 X. Hong, J. Mei, L. Wen, Y. Tong, A. J. Vasileff, L. Wang, J. Liang, Z. Sun and S. Dou, *Adv. Mater.*, 2019, **31**, 1802822.
12 Y. Tsao, M. Lee, E. C. Miller, G. Gao, J. Park, S. Chen, T. Katsumata, H. Tran, L. Wang, M. F. Toney, Y. Cui and Z. Bao, *Joule*, 2019, **3**, 872–884.
13 I. Kovalev, Y. Mikhaylik and T. Weiß, *High energy rechargeable Li–S battery development at Sion Power and BASF*, Li-S Workshop, Dresden, 2013.
14 R. V. Noorden, *Nature*, 2014, **507**, 26–28.
15 J. Balach, J. Linnemann, T. Jaumann and L. Giebeler, *J. Mater. Chem. A*, 2018, **6**, 23127–23168.
16 R. Xu, J. Lu and K. Amine, *Adv. Energy Mater.*, 2015, **5**, 1500408.
17 Q. Pang, X. Liang, C. Kwok and L. F. Nazar, *J. Electrochem. Soc.*, 2015, **162**, A2567–A2576.
18 H. Shi, W. Lv, C. Zhang, D. Wang, G. Ling, Y. He, F. Kang and Q. Yang, *Adv. Funct. Mater.*, 2018, **28**, 1800508.
19 W. Xue , Z. Shi, L. Suo, C. Wang, Z. Wang, H. Wang , K. P. So, A. Mauran , D. Yu, Y. Chen, L. Qie, Z. Zhu, G. Xu , J. Kong and J. Li, *Nat. Energy*, 2019, **4**, 374.
20 M. Naguib, M. Kurtoglu, V. Presser, J. Lu, J. Niu, M. Heon, L. Hultman, Y. Gogotsi and M. W. Barsoum, *Adv. Mater.*, 2011, **23**, 4248.
21 M. Mojtabavi, A. V. Mohammadi, W. Liang, M. Beidaghi and M. Wanunu, *ACS Nano*, 2019, **133**, 3042–3053.
22 B. Anasori, M. R. Lukatskaya and Y. Gogotsi, *Nat. Rev. Mater.*, 2017, **2**, 16098.
23 M. Alhabeb, K. Maleski, B. Anasori, P. Lelyukh, L. Clark, S. Sin and Y. Gogotsi, *Chem. Mater.*, 2017, **29**, 7633–7644.
24 Y. Liu, X. Zhu and L. Pan, *Small*, 2018, **14**, 1803632.
25 B. Li, H. Xu, Y. Ma and S. Yang, *Nanoscale Horiz.*, 2019, **4**, 77–98.
26 Z. Zhang, H. Peng, M. Zhao and J. Huang, *Adv. Funct. Mater.*, 2018, **28**, 1707536.
27 X. Liang, A. Garsuch and L. F. Nazar, *Angew. Chem., Int. Ed.*, 2015, **54**, 3907–3911.
28 D. Rao, L. Zhang, Y. Wang, Z. Meng, X. Qian, J. Liu, X. Shen, G. Qiao and R. Lu, *J. Phys. Chem. C*, 2017, **121**, 11047–11054.
29 Y. Zhao and J. Zhao, *Appl. Surf. Sci.*, 2017, **412**, 591–598.
30 N. Li, Q. Meng, X. Zhu, Z. Li, J. Ma, C. Huang, J. Song and J. Fan, *Nanoscale*, 2019, **11**, 8485–8493.
31 D. Wang, F. Li, R. Lian, J. Xu, D. Kan, Y. Liu, G. Chen, Y. Gogotsi and Y. Wei, *ACS Nano*, 2019, DOI: 10.1021/acsnano.9b03412.
32 H. Lin, D. Yang, N. Lou, S. Zhu and H. Li, *Ceram. Int.*, 2019, **45**, 1588–1594.
33 E. S. Sim, G. S. Yi, M. Je, Y. Lee and Y.-C. Chung, *J. Power Sources*, 2017, **342**, 64–69.
34 X. Liu, X. Shao, F. Li and M. Zhao, *Appl. Surf. Sci.*, 2018, **455**, 522–526.
35 E. S. Sim and Y.-C. Chung, *Appl. Surf. Sci.*, 2018, **435**, 210–215.
36 Z. Xiao, Z. Yang, L. Wang, H. Nie, M. Zhong, Q. Lai, X. Xu, L. Zhang and S. Huang, *Adv. Mater.*, 2015, **27**, 2891–2898.
37 D. Liu, C. Zhang, G. Zhou, W. Lv, G. Ling, L. Zhi and Q. H. Yang, *Adv. Sci.*, 2018, **5**, 1700270.

38 C. Ruan, Z. Yang, H. Nie, X. Zhou, Z. Guo, L. Wang, X. Ding, X. Chen and S. Huang, *Nanoscale*, 2018, **10**, 10999–11005.
39 W. Hua, Z. Yang, H. Nie, Z. Li, J. Yang, Z. Guo, C. Ruan, X. Chen and S. Huang, *ACS Nano*, 2017, **11**, 2209–2218.
40 X. Liang, Y. Rangom, C. Y. Kwok, Q. Pang and L. F. Nazar, *Adv. Mater.*, 2017, **29**, 1603040.
41 W. Bao, L. Liu, C. Wang, S. Choi, D. Wang and G. Wang, *Adv. Energy Mater.*, 2018, **8**, 1702485.
42 H. Tang, W. Li, L. Pan, C. P. Cullen, Y. Liu, A. Pakdel, D. Long, J. Yang, N. McEvoy, G. S. Duesberg, V. Nicolosi and C. Zhang, *Adv. Sci.*, 2018, **5**, 1800502.
43 T. Zhao, P. Zhai, Z. Yang, J. Wang, L. Qu, F. Du and J. Wang, *Nanoscale*, 2018, **10**, 22954–22962.
44 H. Tang, W. Li, L. Pan, K. Tu, F. Du, T. Qiu, J. Yang, C. P. Cullen, N. McEvoy and C. Zhang, *Adv. Funct. Mater.*, 2019, **29**, 1901907.
45 Z. Pourali, M. R. Yaftian and M. R. Sovizi, *Mater. Chem. Phys.*, 2018, **217**, 117–124.
46 M. Li, Y. Zhang, F. M. Hassan, W. Ahn, X. Wang, W. Liu, G. Jiang and Z. Chen, *J. Mater. Chem. A*, 2017, **5**, 21435–21441.
47 Z. Xiao, Z. Yang, Z. Li, P. Li and R. Wang, *ACS Nano*, 2019, **13**, 3404–3412.
48 R. Steudel and T. Chivers, *Chem. Soc. Rev.*, 2019, **48**, 3279–3319.
49 Q. Wang, J. Zheng, E. Walter, H. Pan, D. Lv, P. Zuo, H. Chen, Z. D. Deng, B. Y. Liaw, X. Yu, X. Yang, J. Zhang, J. Liu and J. Xiao, *J. Electrochem. Soc.*, 2015, **162**, A474–A478.
50 W. Bao, D. Su, W. Zhang, X. Guo and G. Wang, *Adv. Funct. Mater.*, 2016, **26**, 8746–8756.
51 W. Bao, X. Xie, J. Xu, X. Guo, J. Song, D. Su, G. Wang and W. Wu, *Chem.–Eur. J.*, 2017, **23**, 12613–12619.
52 J. Song, X. Guo, J. Zhang, Y. Chen, C. Zhang, L. Luo, F. Wang and G. Wang, *J. Mater. Chem. A*, 2019, **7**, 6507–6513.
53 X. Wang, C. Yang, X. Xiong, G. Chen, M. Huang, J. Wang, Y. Liu, M. Liu and K. Huang, *Energy Storage Materials*, 2019, **16**, 344–353.
54 Y. Yao, W. Feng, M. Chen, X. Zhong, X. Wu, H. Zhang and Y. Yu, *Small*, 2018, **14**, 1802516.
55 M. S. Song, S. C. Han, H. S. Kim, J. H. Kim, K. T. Kim, Y. M. Kang, H. J. Ahn, S. X. Dou and J. Y. Lee, *J. Electrochem. Soc.*, 2004, **151**, A791–A795.
56 X. Gao, Y. Xie, X. Zhu, K. Sun, X. Xie, Y. Liu, J. Yu and B. Ding, *Small*, 2018, **14**, 1802443.
57 H. Pan, X. Huang, R. Zhang, D. Wang, Y. Chen, X. Duan and G. Wen, *Chem. Eng. J.*, 2019, **358**, 1253–1261.
58 C. Du, J. Wu, P. Yang, S. Li, J. Xu and K. Song, *Electrochim. Acta*, 2019, **295**, 1067–1074.
59 Y. Zhang, Z. Mu, C. Yang, Z. Xu, S. Zhang, X. Zhang, Y. Li, J. Lai, Z. Sun, Y. Yang, Y. Chao, C. Li, X. Ge, W. Yang and S. Guo, *Adv. Funct. Mater.*, 2018, **28**, 1707578.
60 J. Xiao, *Adv. Energy Mater.*, 2015, **5**, 1501102.
61 Z. Xiao, Z. Li, P. Li, X. Meng and R. Wang, *ACS Nano*, 2019, **13**, 3608–3617.
62 X. Cheng, C. Yan, X. Zhang, H. Liu and Q. Zhang, *ACS Energy Lett.*, 2018, **3**, 1564–1570.
63 E. Peled, D. Golodnitsky and G. Ardel, *J. Electrochem. Soc.*, 1997, **144**, L208–L210.
64 K. Xu, *Chem. Rev.*, 2014, **114**, 11503–11618.
65 Y. Liu, D. Lin, Y. Jin, K. Liu, X. Tao, Q. Zhang, X. Zhang and Y. Cui, *Sci. Adv.*, 2017, **3**, eaao0713.
66 D. Lin, Y. Liu, Z. Liang, H. Lee, J. Sun, H. Wang, K. Yan, J. Xie and Y. Cui, *Nat. Nanotechnol.*, 2016, **11**, 626.
67 B. Li, D. Zhang, Y. Liu, Y. Yu, S. Li and S. Yang, *Nano Energy*, 2017, **39**, 654–661.
68 Y. Su and A. Manthiram, *Chem. Commun.*, 2012, **48**, 8817–8819.
69 Y. Su and A. Manthiram, *Nat. Commun.*, 2012, **3**, 1166.
70 J. He, Y. Chen and A. Manthiram, *Energy Environ. Sci.*, 2018, **11**, 2560–2568.
71 H. Peng, D. Wang, J. Huang, X. Cheng, Z. Yuan, F. Wei and Q. Zhang, *Adv. Sci.*, 2016, **3**, 1500268.
72 X. Qian, L. Jin, D. Zhao, X. Yang, S. Wang, X. Shen, D. Rao, S. Yao, Y. Zhou and X. Xi, *Electrochim. Acta*, 2016, **192**, 346–356.
73 C. H. Chang, S.-H. Chung and A. Manthiram, *J. Mater. Chem. A*, 2015, **3**, 18829–18834.
74 J. Song, D. Su, X. Xie, X. Guo, W. Bao, G. Shao and G. Wang, *ACS Appl. Mater. Interfaces*, 2016, **8**, 29427–29433.
75 J. Jin, C. Lin, W. Zhang, L. Wang, Z. G. Wang, W. Zhao, W. Duan, Z. Zhao and B. Liu, *J. Mater. Chem. A*, 2016, **4**, 5993–5998.
76 L. Yin, G. Xu, P. Nie, H. Dou and X. Zhang, *Chem. Eng. J.*, 2018, **352**, 695–703.
77 R. Fang, S. Zhao, S. Pei, X. Qian, P. Hou, H. Cheng, C. Liu and F. Li, *ACS Nano*, 2016, **10**, 8676–8682.
78 Y. Dong, S. Zheng, J. Qin, X. Zhao, H. Shi, X. Wang, J. Chen and Z. Wu, *ACS Nano*, 2018, **12**, 2381–2388.
79 D. Guo, F. Minga, H. Su, Y. Wu, W. Wahyudi, M. Li, M. N. Hedhili, G. Sheng, L. Li, H. N. Alshareef, Y. Li and Z. Lai, *Nano Energy*, 2019, **61**, 478–485.
80 L. Jiao, C. Zhang, C. Geng, S. Wu, H. Li, W. Lv, Y. Tao, Z. Chen, G. Zhou, J. Li, G. Ling, Y. Wan and Q. Yang, *Adv. Energy Mater.*, 2019, **9**, 1900219.
81 N. Li, Y. Xie, S. Peng, X. Xiong and K. Han, *J. Energy Chem.*, 2020, **42**, 116–125.